Hindawi
Geofluids
Volume 2021, Article ID 5580185, 12 pages
https://doi.org/10.1155/2021/5580185

Research Article

Experimental Investigation of Permeability Evolution on Sandstone in Triaxial and Long-Term Dissolution Experiment

Ji Shi, Jianhua Zhang, Chunyang Zhang, Tingting Jiang, and Gang Huang

Mining engineering, Wuhan University of Technology, 430070, China

Correspondence should be addressed to Ji Shi; shiji314@outlook.com

Received 12 January 2021; Revised 28 January 2021; Accepted 9 February 2021; Published 22 February 2021

Academic Editor: Yu Wang

The temporal permeability and damage evolutions of low-permeability sandstone cores during triaxial and long-term dissolution experiments were measured using a triaxial-flow system. Three triaxial experiments were performed on sandstone cores having initial permeability ranging from 78×10^{-18} m^2 to 120×10^{-18} m^2. Two sets of long-term dissolution experiments were conducted on cracked sandstone cores. All dissolution experiments were performed at room temperature and using a 10 g/L H_2SO_4 and 0.2 g/L H_2O_2 input solution. Permeability evolution was determined using Darcy's law. The cores experienced an average increase of 25% in permeability in the dissolution experiment and 900%~1500% increase at the end of the experiment. The dissolution was fairly homogeneous during the long-term experiments whether on the 1 mm scale or the 10 μm scale. The relationship between damage and permeability was speculated and its correlation coefficient has been proved to be close to 1. These results suggest that hydraulic fracturing works well in permeability increase in low-permeability sandstone reservoir.

1. Introduction

Resource exploitation and engineering construction are influenced by the mechanical properties of rocks/soils [1–3]. Therefore, in some cases, their mechanical properties need to be changed according to requirements for exploitation [4–6]. How to increase the permeability of orebody artificially is the research front on many scientific topics such as petroleum engineering [7, 8], oil and gas storage [9–11], and in situ leaching mining.

Sandstone-hosted uranium deposits refer to the epigenetic and post exogenic deposits generated in sandstone, glutenite, and other clastic rocks. It is one of the earliest discovered and the most widely distributed uranium deposits in the world [12]. Those fine qualities of sandstone-hosted uranium deposits such as, for instance, medium-grade ore with a general value of about 0.1%~0.2%, high-quality ore, and stable occurrence, contribute to its great industrial value. Economic benefits of the deposits could be greatly improved by utilizing in situ leaching mining [13]. Low-permeability sandstone reservoir accounts for more than 50% of total reserves. However, the physical properties of low-permeability sandstone, like developed microfissures, narrow pore radius, and small flow path, will lead to significant abrupt change in permeability in engineering process. Permeability is one of the most important evaluation criteria of exploitation and financial performance. Therefore, the permeability evolution in consolidated sandstone in engineering project is a research of great practical significance and requiring further study.

Many scholars have studied the permeability evolution of sandstone under different conditions. Lufeng et al. introduced a method to quantitatively evaluate the core permeability damage from a macroscopic perspective [7]. Liu et al. conducted an experiment to explore the gas porosity and permeability variation of sandstone at different levels of water saturation in loading-unloading cycles [14]. Odumabo investigated the fracturing fluid leakoff in low-permeability sandstones [11]. Zeng designed a simulation experiment for gas migration and accumulation in natural consolidated sandstone [15]. Fu et al. tried to explore the stress dependence of the absolute and relative permeabilities of some consolidated sandstones [9]. Wojtacki et al. presented a numerical method for estimating the stiffness-to-porosity relationships for evolving microstructures of Fontainebleau

sandstone [16]. These studies provide part of the theoretical basis for permeability evolution in low-permeability sandstone reservoir. In addition to the influence of engineering projects, the degradation of rock caused by leaching solution would also affect the permeability evolution in sandstone. Colón investigated the effect of dissolution on sandstone permeability, with the solution of NaOH (pH = 11.4) [17]. Mecchia et al. developed a hybrid model to estimate fracture karstification in quartz sandstone [18]. McKinley et al. calculated how porosity and permeability vary spatially with grain size, sorting, cement volume, and mineral dissolution in fluvial Triassic sandstones [19]. These studies have significant insights into the permeability evolution in sandstone under various states. At present, relatively few studies have explored long-term permeability evolution in sandstone during physicochemical processes. However, the long-term chemical reaction between leaching solution and acid soluble minerals in sandstone [20] will reduce strength and increase the permeability considerably [21].

The objectives of this study are to explore the permeability evolution and evaluate the damage caused by chemical reaction together with hydraulic fracturing, using triaxial experiment and SEM analysis. We establish a model and derive the equations to describe the relationship between damage and permeability in triaxial experiment and dissolution experiment.

2. Materials and Methods

2.1. Core Sample Preparation. Sample preparation is very important in the research process, which determines the reliability of the final results. The core samples were collected from the core of No. PD03 borehole in 2# stope of a uranium mine in Northwest China. The deposit is in the south of the Ili basin, the tectonic position of which is the east of the Ili microplate sandwiched by the Kazakhstan plate and the Tarim plate. The uranium metallogenic region is divided into two parts: the "roll" and the "tail." The "roll" part is 45 m~205 m in length and relatively stable. The ore body is mainly composed of medium-coarse-grained and medium-fine-grained sandstone, most of which are grey, dark grey, and black grey. Clastic materials account for about 84.2% of the ore, while silty clay is about 15.77%. The main components of the clastic materials are quartz (51%~79%), cuttings (8%~20%), and feldspar (5%~15%). There is no easily-dilating montmorillonite in clay. The accessory minerals and authigenic minerals are mainly titanite (0.48%), pyrite (0.35%), limonite (0.22%), and pitchblende (0.18%). The effective porosity of the sandstone-hosted uranium ore is 12.2-13.1%, the main components of which are 76.38% SiO_2, 11.87% Al_2O_3, and 1.45% Fe_2O_3, as well as trace amounts of MnO, MgO, and CaO. Insoluble or difficultly soluble minerals account for 95.3% of the ore, and soluble minerals account for 1.5%~5.5%.

Refer to the rock mechanics standard GB/T50266-2013, the core samples are cylindrical cores with a diameter of 50 mm and a length of 100 mm. The diameter error of the core sample is no more than 0.3 mm, and the vertical deviation between the end face and the axis of the core sample is no more than 0.25°. Typical core samples are shown in Figure 1. All the core samples were weighed up and recorded at first. Put all the core samples into drying oven and keep constant temperature drying at 105°C for 24 h. Take out the core samples and put them into a desiccator until they cool to room temperature. Record weight of every core sample, and duplicate the above steps until the D value of two adjacent weight records is no more than 0.1% of the last record. Put all the dried core samples into the vacuum saturation device, and make sure they are completely submerged in water. Set vacuum pressure as 100 kPa, pumping air for at least 6 h until no bubbles escape from water. Then, keep the core samples at atmospheric pressure in the vacuum saturation device for another 4 h. Make sure each core sample is fully saturated with water [22–27].

2.2. Experimental Method. TAW-2000 was utilized in experiments conducted in this study; it is a triaxial pressure-seepage system, as shown in Figure 2. The instrument can provide a maximum axial load of 2000 kN and a maximum confining pressure of 80 MPa. The measurement range of radial and axial displacement is 0~4 mm and 0~8 mm, and the resolution of pressure measurement is 1/180000. The system is equipped with a full digital servo controller, oil pump, and water pump that independently control axial pressure, confining pressure, and hydrostatic pressure. The axial strain is measured by the axial extensometer and linear variable differential transformer (LVDT), and the radial strain is measured by four radial strain gauges fixed to the center of the core sample, the measurement accuracy is ±0.5% FS. All displacement, stress, and strain data are displayed on the computer control system in real time [6, 28–42].

This experiment is divided into two main parts. In the first one, various confining pressure triaxial experiments were conducted. First, the saturated core sample was placed in the cylindrical chamber as shown in Figure 2 with confining pressure P_c (5 MPa, 10 MPa, and 15 MPa) and pore pressure P_p (4 MPa). The axial displacement increased at 0.02 mm/min until the ultimate strength was reached; the computer automatically recorded all the data including axial strain and circumferential strain. The purpose of part one is to gain an improved understanding of the permeability evolution of sandstone in triaxial experiment. In the second one, we conducted long-term flow experiments for 12 days. Two groups of saturated core samples were prepared, and each group contains eight core samples, similar to the first part except for confining pressure P_c which remained 5 MPa in both groups at first. The axial pressure stopped increasing and remained constant as soon as it reached ultimate strength. Core samples in group two were flooded with solution prepared before, while those in group one were flooded with double-distilled water as a control group. The input solution was pumped into the cell at a constant fluid flow rate until a stable differential pore pressure was achieved. Input solution for group two was prepared from reagent grade H_2SO_4 diluted in double-distilled water and concentrated reagent-grade H_2O_2 to produce a solution (10 g/L H_2SO_4 and 0.2 g/L H_2O_2). Record permeability every 12 h for both groups. Pore pressure increased from 4 MPa to

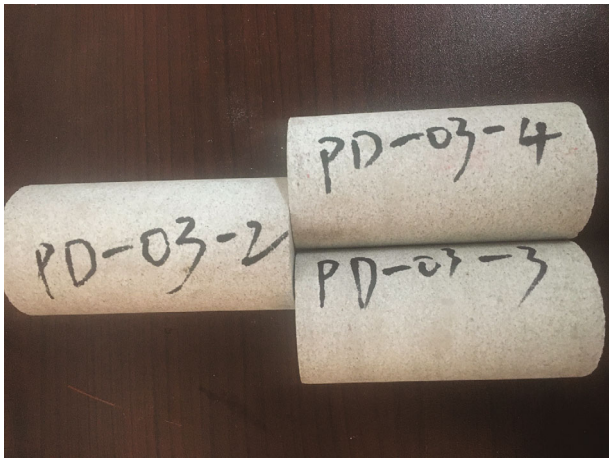

Figure 1: Typical sandstone core samples.

6 MPa on the 6th day. The purpose of part two is to investigate permeability evolution of sandstone in dissolution experiment after it reaches ultimate strength, thus providing feasibility assessment in permeability increase in low-permeability sandstone reservoir.

The steady-state method could be used for the measurement of rocks with relatively high permeability. According to Darcy's law, the permeability of the core sample could be calculated by measuring the liquid volume of the core sample in a period of time. The calculation method is as follows:

$$k = \frac{Q\mu L}{\Delta p A}, \tag{1}$$

where Q is the liquid flow rate per unit time, μ refers to viscosity coefficient of liquid, Δp represents pore pressure difference at both ends, A is cross-sectional area, and L is length of core sample.

The temporal porosity change during the dissolution of a sandstone core can be evaluated from the total soluble minerals removed by the reactive fluid in accord with

$$\phi_t = \phi_0 + \frac{V_m}{V_{\text{core}}} Q \int_{t=t_0}^{t} \Delta C_{\text{mine}} dt, \tag{2}$$

where ϕ_t represents porosity of the core at time t, ϕ_0 refers to the initial core porosity, t_0 denotes the time at the beginning of the experiment, V_m is molar volume of soluble minerals, and V_{core} denotes the total core volume. ΔC_{mine} refers to the difference in soluble minerals molal concentration between the inlet and the outlet solutions at steady-state, and Q corresponds to the mass flow rate of the reactive fluid.

Many equations aimed at estimating the permeability evolution of porous materials are based on permeability/porosity correlations. A commonly used correlation is expressed as follows:

$$k = k_0 \left(\frac{\phi}{\phi_0}\right)^n, \tag{3}$$

where k_0 stands for the permeability at the beginning of the dissolution experiment at an initial porosity of ϕ_0. The exponent n is a constant, which is usually 2 or greater. It can be obtained by a curve-fitting procedure.

3. Results and Discussion

After the test, data analysis can be carried out, which is an important work in studies [5, 28, 43–59]. The temporal evolution of permeability and mechanical property during the various confining pressure triaxial experiments performed in TAW-2000 is illustrated in Figure 3. Three core samples experienced an initial permeability decrease followed by a continuous permeability increase during the experiments, which are attributed to fracture propagation. Permeability decreased along with pore throats size at the beginning of the experiment. Then, plastic deformation under dynamic loading in the core sample contributes to the occurrence of fractures, and volumetric strain began to decrease. The overall permeability increases during the experiments for samples 1, 2, and 3 in part one, which had initial permeability of 95×10^{-18} m^2, 87×10^{-18} m^2, and 82×10^{-18} m^2, were 1500, 1000, and 900%, respectively. These different permeability increase rates are attributed in the present study to the confining pressure. For example, the permeability of core sample 1 increases at a faster rate than the other two core samples, which may stem from the relatively low confining pressure.

Mechanical properties of rock in triaxial experiment such as elastic modulus, deformation modulus, and Poisson's ratio are different from those in uniaxial experiment. The elastic modulus E and Poisson's ratio μ can be expressed as follows:

$$\begin{aligned} E &= \frac{\sigma_1 - 2\mu\sigma_3}{\varepsilon_1}, \\ \mu &= \frac{B\sigma_1 - \sigma_3}{\sigma_3(2B-1) - \sigma_1}, \\ B &= \frac{\varepsilon_3}{\varepsilon_1}, \end{aligned} \tag{4}$$

where σ_1 stands for axial stress, σ_3 represents confining pressure, and ε_1 and ε_3 refer to axial and circumferential strain.

The volume strain of rock could not be measured directly in triaxial experiment, and hence, it is approximately expressed by the following formula:

$$\varepsilon_v = \varepsilon_1 + 2\varepsilon_3, \tag{5}$$

where ε_v designates volume strain and ε_1 and ε_3 represent axial and circumferential strain, respectively.

The circumferential strain can be regarded as the combination of two parts, namely elastic volume strain and the plastic strain result from rock failure. The elastic volume strain is shown as follows:

$$\varepsilon_2^e = \frac{1 - 2\mu}{E}(\sigma_1 + 2\sigma_3). \tag{6}$$

(a)

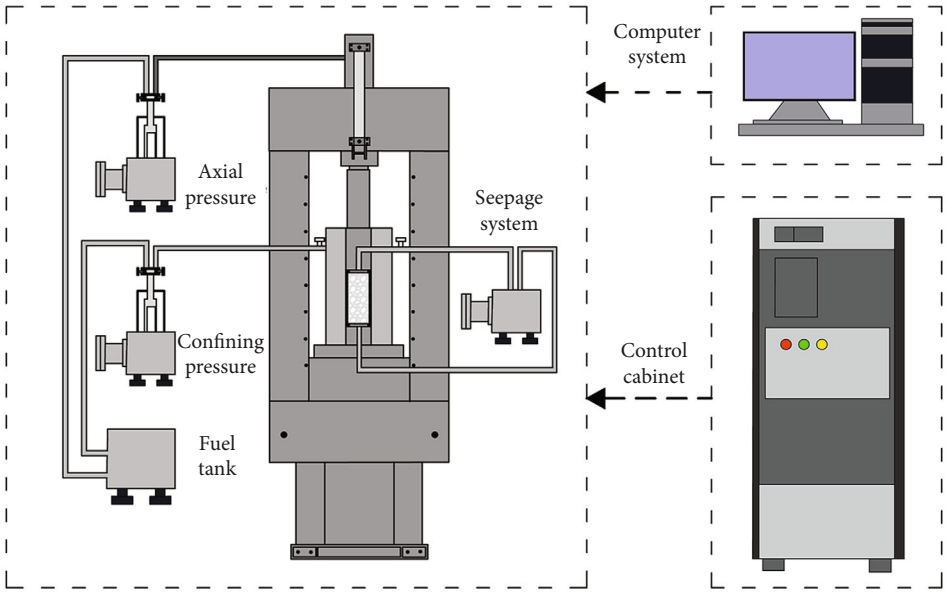

(b)

Figure 2: High temperature and high-pressure triaxial system. (a) Physical photograph. (b) Schematic diagram.

By subtracting the elastic volume strain from the total circumferential strain, the plastic strain result from crack ε_2^c, which reflects the propagation of axial crack, could be obtained, as follows:

$$\varepsilon_3 - \varepsilon_3^e = \varepsilon_3^c. \tag{7}$$

It can be seen from Figure 3 that there is a correlation between the crack circumferential strain and permeability. At the beginning of the experiment, microcracks in the core sample disappear and no new cracks grow. The increase of volume strain mainly stems from elastic deformation. Therefore, almost all circumferential strain is elastic strain, and the crack circumferential strain was almost nonexistent. The increase of elastic strain corresponds reasonably well with the small decline in permeability. As axial stress increases and reaches the yield strength and ultimate strength, cracks begin to grow and coalesce until they merge into a sliding surface and cause rock failure. Crack circumferential strain increases rapidly at first and then shows no more change. Volumetric strain experiences a parabolic growth and the new fractures dramatically increase the permeability. The temporal evolution of permeability and crack circumferential strain are not synchronized; in general, the increase of permeability lags behind that of crack circumferential strain.

In the second part of the experiment, we conducted a long-term dissolution experiment to explore the temporal evolutions of permeability; we recorded permeabilities of 2 groups every 12 hours for 12 days. Results in long-term flow experiments are illustrated in Figure 4.

It can be seen in Figure 4(a) that most core samples experienced a decrease in permeability at the beginning except for

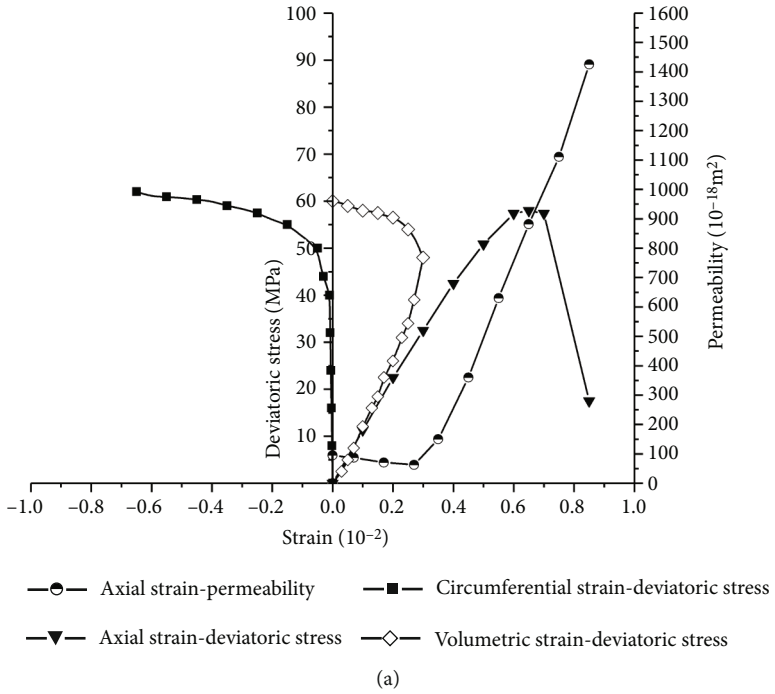

(a)

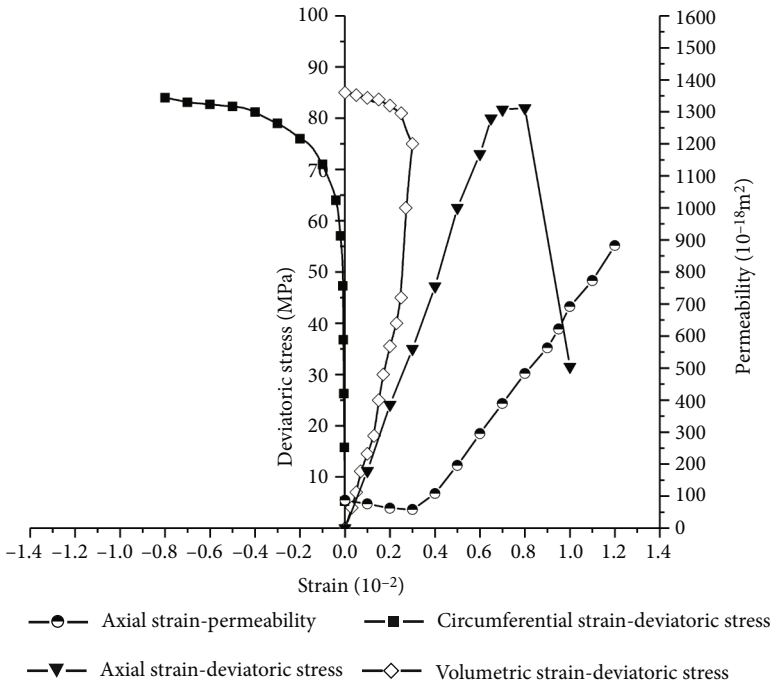

(b)

Figure 3: Continued.

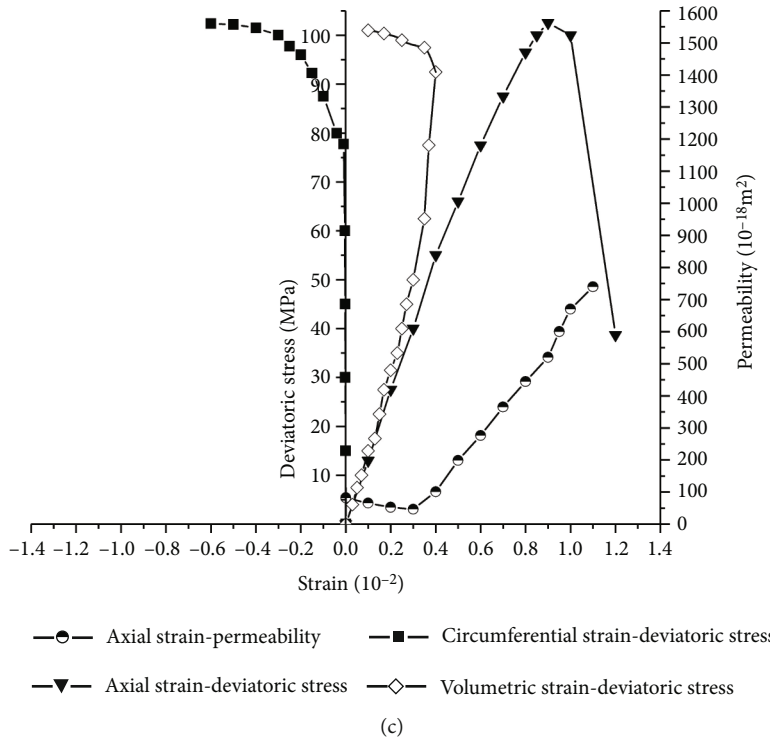

Figure 3: Temporal evolution of permeability and mechanical property during the various confining pressure triaxial experiments. (a) 5 MPa. (b) 10 MPa. (c) 15 MPa.

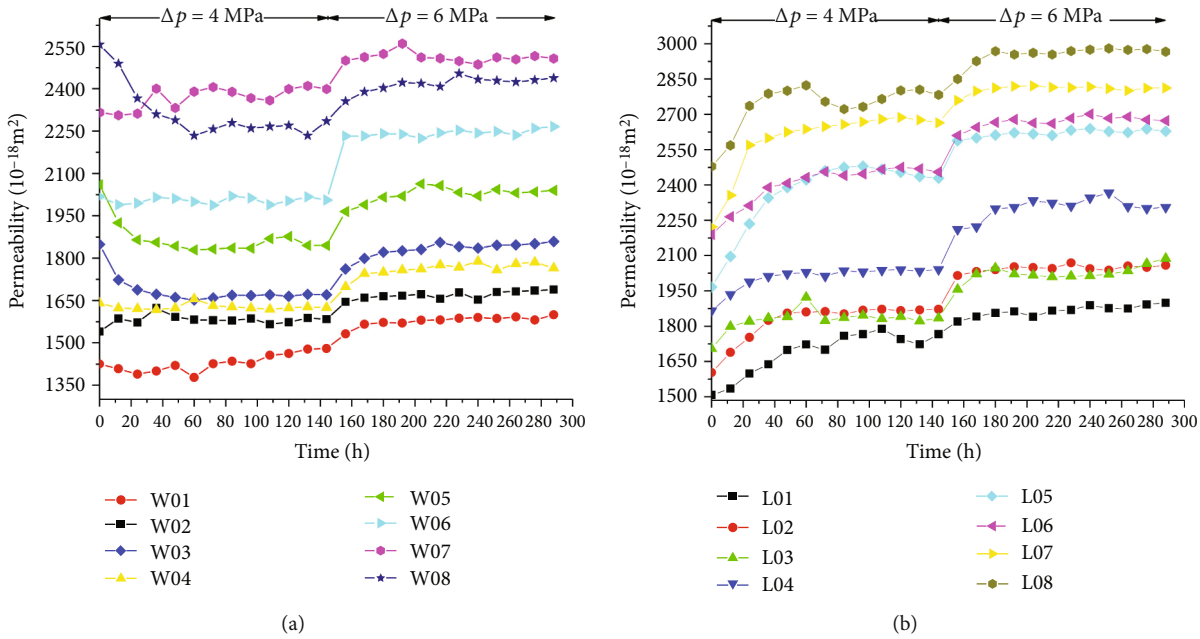

Figure 4: Temporal evolutions of permeability during the sandstone long-term dissolution experiments performed during the present study. (a) Group 1. (b) Group 2.

core sample W02, and a 15% decrease is achieved in core sample W08. Permeabilities of all cores tended to remain constant in about 48 hours and 72 hours. The decrease may stem from the tiny rock fragments that blocking the pore throats, which at the same time prevent the pore throats from closing completely. Pore pressure changed from 4 MPa to 6 MPa on the 6th day, most core samples experienced a slightly increase except for core sample W06. This substantial permeability growth may stem from the rock fragments redistribution in fractures and pore throats.

The permeability evolution as a function of time during the long-time core dissolution experiment can be assessed with the aid of Figure 4(b). An overall average increase of 17% in permeability can be observed in the first part of the experiment, the largest increase is 26% and the smallest is 9%. Permeabilities of most cores tend to remain constant within 90 hours at most, including some short-term fluctuations in core samples L08 and L03. Pore pressure changed from 4 MPa to 6 MPa on the 6^{th} day; all cores experienced a slight permeability increase from 3% to 13%.

The variations of measured permeabilities of group 2 are compared with those of group 1. At the end of the experiment, core samples of group 2 experienced a large permeability increase, which ranges from 18% for core sample L03 to 33% for core sample L05. Group 1 has an average increase of 5%, and permeabilities of core sample W03 and W05 are almost the same as its beginning separately.

Two conclusions can be drawn from the observations above. First, permeability evolution of cracked core sample during the long-term dissolution is affected by various factors, including location and direction of fractures and pore throats, tiny rock fragments, and pore pressure. These various factors can cause uncertainty in permeability increase. Secondly, dissolution can lead to an average increase of 25% permeability among cracked core samples.

Carlos et al. [17] conducted a long-term dissolution experiment of four Fontainebleau sandstone cores. Photomicrographs were taken of the full cross section of core sample 3 before and following the percolation experiments. Representative examples are illustrated in Figure 5.

This grain dissolution experiment was performed in a 0.1 mol/kg NaOH aqueous solution. The initial porosity of the core ranged from 7.03 to 8.63%, whereas those of the postexperiment ranged from 13.2 to 15.8%. It can be seen that quartz grain size and porosity distribution appear to be homogeneous on the 1 mm scale.

Yao et al. [28] explored permeability characteristics of sandstone in different chemical solutions. The SEM graphs of samples are illustrated in Figure 6.

This dissolution experiment was performed in 6 g/L H_2SO_4 acid solution (pH = 2). It appears that the surface of the sample was generally smooth on the 10 μm scale before the dissolution, whereas the asperities of the postexperiment suggest the chemical reactions between acid and sandstone. Loads of pores and pore throats appeared on the surface, and the gap opening increases because the tiny fragments attached to the surface may slide down as the solution flows. The permeability increase may stem from the reasons mentioned above.

Several conclusions can be drawn from these observations. First, as all reactive fluids were the same temperature, pH, and H_2SO_4 concentration, and all core samples were fully saturated with water initially, these different permeability increase rates are attributed in the present study to the distinct fracture propagation and pore throats of each core sample. Secondly, the dissolution was fairly homogeneous during the long-term experiments whether on the 1 mm scale or the 10 μm scale. Thirdly, permeability increase stem from both the macroscopic fracture propagation and microscopic dissolution.

We consider the overall change of rock as damage to help describe the evolution of permeability during rock failure and dissolution. In order to describe the relationship between damage and permeability, we introduced a damage model and strength criterion for rock in triaxial experiment. Based on Terzaghi formula and hypothesis of strain equivalence, the effective stress tensor σ_e in joint action of rock failure and dissolution is defined as follows:

$$\sigma_e = \frac{\bar{\sigma} - p_w \delta}{1 - D}, \tag{8}$$

where $\bar{\sigma}$ refers to stress tensor, p_w represents pore pressure, δ is unit second-order tensor, and D represents degree of damage in rock materials. The degree of damage is related to the number and size of pores, pore throats, and fractures in rock materials, which directly affect the strength and permeability of rock. It is assumed that the strength of microelement in rock materials follows the power function distribution, and its probability density function is

$$P(F) = \frac{m}{F_0}\left(\frac{F}{F_0}\right)^{m-1}. \tag{9}$$

m, F_0 is the parameter in the distribution function which could be obtained by fitting of experimental data.

$$D = \int_0^F P(x)dx = \left(\frac{F}{F_0}\right)^m, \tag{10}$$

where $F \geq 0$. The three-dimensional constitutive relation of strength of microelement following normal distribution could be obtained.

$$\sigma_1 = E\varepsilon_1\left[1 - \left(\frac{F}{F_0}\right)^m\right] + \mu(\sigma_2 + \sigma_3). \tag{11}$$

where E, μ refers to elastic modulus and Poisson's ratio of rock, respectively, ε_1 represents axial strain, σ_1 is axial stress, and σ_2 and σ_3 are confining pressure.

According to the generalized Hooke's law, the relationship between the axial elastic modulus and Poisson's ratio of rock in triaxial experiment is as follows:

$$\varepsilon_1 = \frac{1}{E}[\sigma_1 - \mu(\sigma_2 + \sigma_3)]. \tag{12}$$

Combined with the formula mentioned above, the stress-strain relationship of rock in seepage-triaxial experiment could be obtained:

$$\sigma_1 = E\varepsilon_1(1 - D) + 2\mu\sigma_3 + (1 - 2\mu)p_w. \tag{13}$$

Loads of experimental results show that Mohr-Coulomb criterion satisfies the yield and failure characteristics of rock materials. However, the yield surface in the main stress space is a hexagonal pyramid with a sharp tip, which makes it quite difficult to calculate, and the effect of pore pressure is not

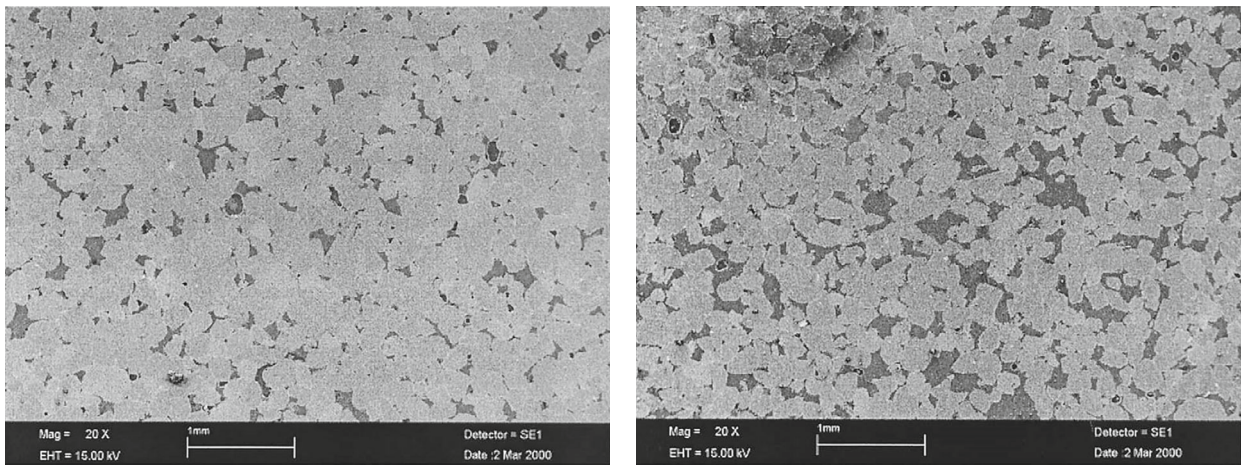

(a) (b)

Figure 5: Photomicrographs of core sample 3 in research of Carlos et al. (a) before and (b) following its dissolution.

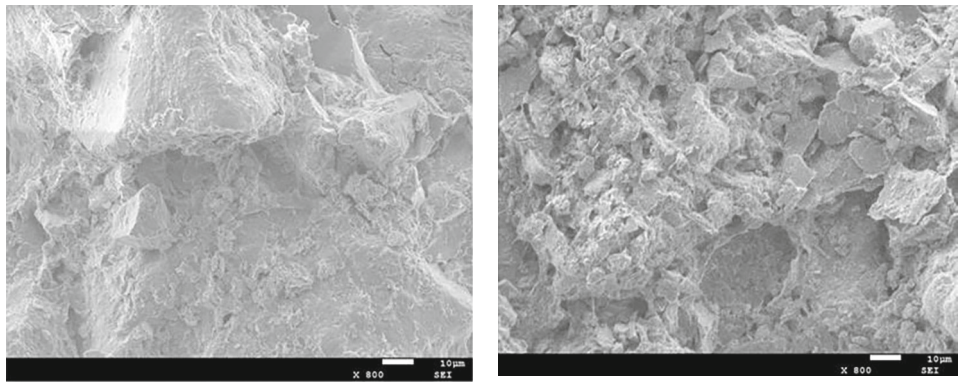

(a) (b)

Figure 6: SEM graphs of sandstone core samples in research of Yao et al. (a) before and (b) following its dissolution.

considered. The yield criterion proposed by Drucker and Prager contains the effect of pore pressure, and its yield surface is a circle tangent to the hexagon in Mohr-Coulomb criterion. This criterion is as follows:

$$f(\sigma) = \alpha_0 I_1 + \sqrt{J_2}, \tag{14}$$

where I_1 is first invariant of stress tensor

$$I_1 = \sigma_1 + \sigma_2 + \sigma_3. \tag{15}$$

J_2 is the second invariant of deviatoric stress

$$J_2 = \frac{1}{6}\left[(\sigma_1 - \sigma_2)^2 + (\sigma_2 - \sigma_3)^2 + (\sigma_1 - \sigma_3)^2\right],$$
$$\alpha_0 = \frac{\sin\varphi}{\sqrt{9 + 3\sin^2\varphi}}. \tag{16}$$

φ is the angle of internal friction.

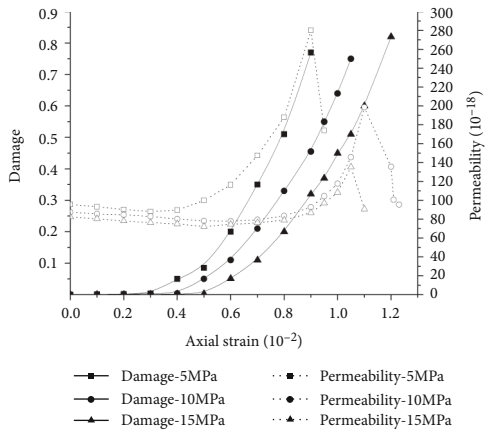

Figure 7: Permeability and damage evolution in the first part of the experiment.

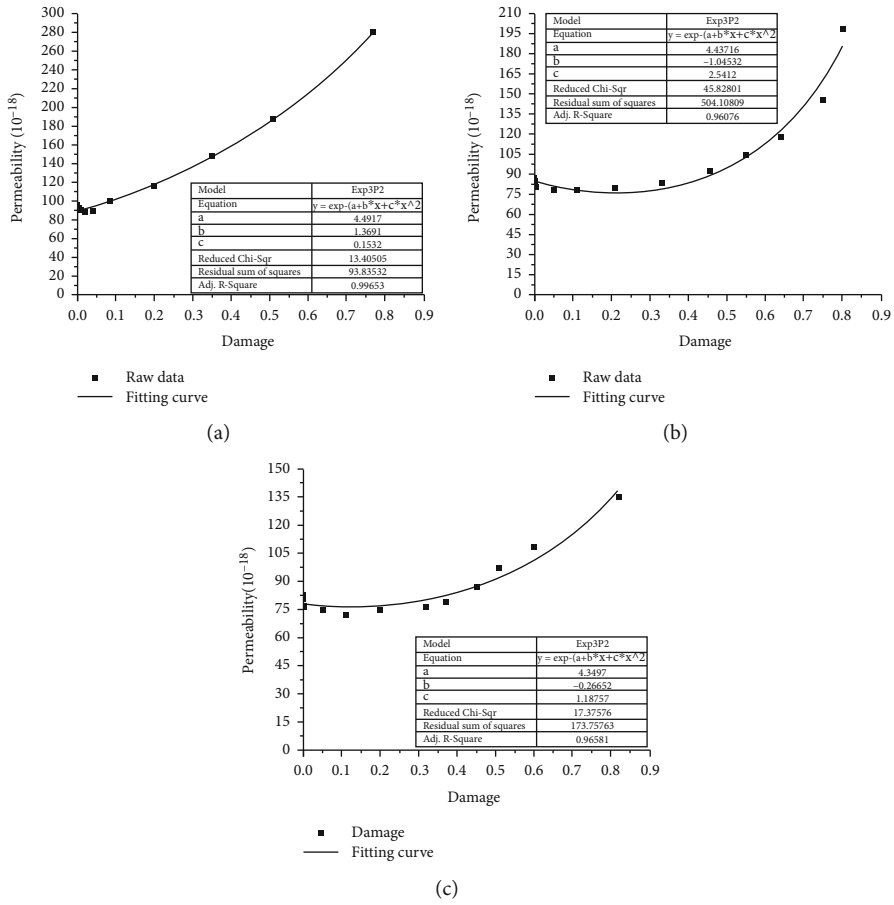

Figure 8: Fitting curve of the relationship between damage and permeability. (a) Confining pressure is 5 MPa. (b) Confining pressure is10 MPa. (c) Confining pressure is 15 MPa.

Before the experiment started, the initial strain ε_0 due to confining pressure is expressed as follows:

$$\varepsilon_0 = \frac{1-2\mu}{E}(\sigma_3 - p_w). \tag{17}$$

The experimentally measured axial strain ε_t plus the initial strain is the total strain ε_1

$$\varepsilon_1 = \varepsilon_0 + \varepsilon_t. \tag{18}$$

Based on the above formulas, the functional relation between stress and damage can be obtained:

$$\sigma_d = [(1-2\mu)(\sigma_3 - p_w) + E\varepsilon_t]\left[1 - \left(\frac{F}{F_0}\right)^m\right] + (2\mu - 1)\sigma_3 + (1-2\mu)p_w. \tag{19}$$

Transform the above formula as follows:

$$D = \left(\frac{F}{F_0}\right)^m = \frac{E\varepsilon_t - \sigma_d}{E\varepsilon_t + (1-2\mu)\sigma_3 - p_w}. \tag{20}$$

According to the above formula and experimental data, the permeability and damage evolution is shown in Figure 7.

It can be seen from the figure that, at the beginning of the experiment permeability decreased slightly, while damage almost remained constant. This suggests that the opening of pores and pore throats decreased and few fractures were generated in this period. Then, damage started to increase while the evolution of permeability varies according to confining pressure. Core sample 1 experienced a synchronous increase of permeability and damage, while permeability increases of core sample 2 and 3 lag behind their damage increase, respectively. This may stem from the fact that once the new fractures generated inside the core sample, gap opening tended to decrease or be gone in a short time due to confining pressure.

According to the evolution of permeability and damage in the first part of the experiment, it can be speculated that the damage has an exponential relationship with permeability. A hypothesis of the relationship between damage and permeability was made as follows:

$$K = \exp\left(a + bD + cD^2\right), \tag{21}$$

where K is permeability, order of magnitude is 10^{-18}, D refers to damage, and a, b, and c are undetermined parameters. An exponential function curve-fitting procedure is conducted, as shown in Figure 8.

The results show that the relationship between damage and permeability remained exponential before permeability reaches a maximum value. The average correlation coefficient of each fitting curve is 0.972, and the highest value is 0.99653, which indicates that the fitting function correlates well with the experiment data. Once the permeability reaches the maximum value, with the continuous increase of axial strain, the closing of the sliding surface will lead to the decrease of permeability and the increase of rock damage continually. In real engineering practices, the cost and time to conduct large and long-term experiment to evaluate the geological parameters tend to be very high. In this paper, we establish the damage model and verify the hypothesis of the relationship between damage and permeability. Thus, by conducting a series of experiments, the permeability evolution of sandstone rock could be obtained. The derived equations could save loads of time as well as cost.

4. Conclusions

In this study, the core sample of a Uranium mine in Northwest China and TAW-2000 high-temperature and high-pressure triaxial experiment system developed by Wuhan University of Science and Technology were used. The experiment was divided into two parts; in the first part, we explored the temporal evolution of permeability and mechanical property in triaxial experiment with different confining pressure; in the second part, long time dissolution experiment was conducted; we established the relationship between damage and permeability and evaluated the correlation coefficient. Several conclusions are made:

(1) Permeability evolution of cracked core sample during the long-term dissolution is affected by various factors, including location and direction of fractures and pore throats, tiny rock fragments, and pore pressure. These various factors can cause uncertainty in permeability increase. Dissolution can lead to an average increase of 25% permeability in the second part of the experiment

(2) An average increase of 900%~1500% on permeability was observed in core samples at the end of the experiment, which indicates that hydraulic fracturing using solution works well in permeability increase in low-permeability sandstone deposit. Joint action of hydraulic fracturing and chemical reaction ensures that permeability increases in a reasonable interval

(3) As all reactive fluids were the same temperature, pH, and H_2SO_4 concentration, and all core samples were fully saturated with water initially, the different permeability increase rates are attributed in the present study to the distinct fracture propagation and pore throats of each core sample. According to the previous research and SEM graphs, the dissolution was fairly homogeneous during the long-term experiments whether on the 1 mm scale or the 10 μm scale. Therefore, permeability increase stem from both the macroscopic fracture propagation and microscopic dissolution

(4) The function between damage and permeability works well in predicting permeability evolution before it reaches the maximum value. It provides a way for low-permeability sandstone deposits to evaluate the effect of permeability increase with less experiments and investment.

Data Availability

The permeability and dissolution data used to support the findings of this study are included within the article.

Conflicts of Interest

The authors declare that there is no conflict of interest regarding the publication of this paper.

Acknowledgments

This research was funded by the National Natural Science Foundation of China (Grant No. 51804236 and Grant 51804235).

References

[1] C. Zhang, C. Pu, R. Cao, T. Jiang, and G. Huang, "The stability and roof-support optimization of roadways passing through unfavorable geological bodies using advanced detection and monitoring methods, among others, in the Sanmenxia Bauxite Mine in China's Henan Province," *Bulletin of Engineering Geology and the Environment*, vol. 78, no. 7, pp. 5087–5099, 2019.

[2] Y. Zhao, Y. Wang, and L. Tang, "The compressive-shear fracture strength of rock containing water based on Druker-Prager failure criterion," *Arabian Journal of Geosciences*, vol. 12, p. 452, 2019.

[3] H. Lin, X. Ding, R. Yong, W. Xu, and S. Du, "Effect of non-persistent joints distribution on shear behavior," *Comptes Rendus Mecanique*, vol. 347, no. 6, pp. 477–489, 2019.

[4] X. Fan, K. Li, H. Lai, Y. Xie, R. Cao, and J. Zheng, "Internal stress distribution and cracking around flaws and openings of rock block under uniaxial compression: a particle mechanics approach," *Computers and Geotechnics*, vol. 102, pp. 28–38, 2018.

[5] Y. Wang, P. Guo, H. Lin et al., "Numerical analysis of fiber-reinforced soils based on the equivalent additional stress concept," *International Journal of Geomechanics*, vol. 19, article 0401912211, 2019.

[6] C. Zhang, Y. Wang, and T. Jiang, "The propagation mechanism of an oblique straight crack in a rock sample and the effect of osmotic pressure under in-plane biaxial compression," *Arabian Journal of Geosciences*, vol. 13, p. 736, 2020.

[7] Z. Lufeng, Z. Fujian, Z. Shicheng, L. Zhun, W. Jin, and W. Yuechun, "Evaluation of permeability damage caused by drilling and fracturing fluids in tight low permeability sandstone reservoirs," *Journal of Petroleum Science and Engineering*, vol. 175, pp. 1122–1135, 2019.

[8] C. Zhang, P. Zou, Y. Wang, T. Jiang, H. Lin, and P. Cao, "An elasto-visco-plastic model based on stress functions for

deformation and damage of water-saturated rocks during the freeze-thaw process," *Construction and Building Materials*, vol. 250, no. 118862, p. 118862, 2020.

[9] X. Fu, F. Agostini, F. Skoczylas, and L. Jeannin, "Experimental study of the stress dependence of the absolute and relative permeabilities of some tight gas sandstones," *International Journal of Rock Mechanics and Mining Sciences*, vol. 77, pp. 36–43, 2015.

[10] B. Ghanbarian, C. Torres-Verdín, and T. H. Skaggs, "Quantifying tight-gas sandstone permeability via critical path analysis," *Advances in Water Resources*, vol. 92, pp. 316–322, 2016.

[11] S. M. Odumabo, Z. T. Karpyn, and L. F. Ayala H, "Investigation of gas flow hindrance due to fracturing fluid leakoff in low permeability sandstones," *Journal of Natural Gas Science and Engineering*, vol. 17, pp. 1–12, 2014.

[12] Y. Cheng, S. Wang, R. Jin, J. Li, C. Ao, and X. Teng, "Global Miocene tectonics and regional sandstone-style uranium mineralization," *Ore Geology Reviews*, vol. 106, pp. 238–250, 2019.

[13] S. Akhtar, X. Yang, and F. Pirajno, "Sandstone type uranium deposits in the Ordos Basin, Northwest China: a case study and an overview," *Journal of Asian Earth Sciences*, vol. 146, pp. 367–382, 2017.

[14] S. Liu, H. Wang, W. Xu, and Z. Xiang, "The influence of water saturation and confining pressure to gas porosity and permeability of sandstone," *Environmental Earth Sciences*, vol. 78, no. 6, p. 182, 2019.

[15] J. Zeng, Y. Zhang, S. Zhang, J. Qiao, X. Feng, and S. Feng, "Experimental and theoretical characterization of the natural gas migration and accumulation mechanism in low-permeability (tight) sandstone cores," *Journal of Natural Gas Science and Engineering*, vol. 33, pp. 1308–1315, 2016.

[16] K. Wojtacki, L. Daridon, and Y. Monerie, "Computing the elastic properties of sandstone submitted to progressive dissolution," *International Journal of Rock Mechanics and Mining Sciences*, vol. 95, pp. 16–25, 2017.

[17] C. F. J. Colón, E. H. Oelkers, and J. Schott, "Experimental investigation of the effect of dissolution on sandstone permeability, porosity, and reactive surface area[1]," *Geochimica Et Cosmochimica Acta*, vol. 68, no. 4, pp. 805–817, 2004.

[18] M. Mecchia, F. Sauro, L. Piccini, A. Columbu, and J. De Waele, "A hybrid model to evaluate subsurface chemical weathering and fracture karstification in quartz sandstone," *Journal of Hydrology*, vol. 572, pp. 745–760, 2019.

[19] J. M. McKinley, P. M. Atkinson, C. D. Lloyd, A. H. Ruffell, and R. H. Worden, "How porosity and permeability vary spatially with grain size, sorting, cement volume, and mineral dissolution in fluvial Triassic sandstones: the value of geostatistics and local regression," *Journal of Sedimentary Research*, vol. 81, no. 11-12, pp. 844–858, 2011.

[20] M. I. Leybourne and E. M. Cameron, "Groundwater in geochemical exploration," *Geochemistry-Exploration Environment Analysis*, vol. 10, no. 2, pp. 99–118, 2010.

[21] M. Taneez and C. Hurel, "A review on the potential uses of red mud as amendment for pollution control in environmental media," *Environmental Science and Pollution Research*, vol. 26, no. 22, pp. 22106–22125, 2019.

[22] Y. Wang, W. K. Feng, R. L. Hu, and C. H. Li, "Fracture evolution and energy characteristics during marble failure under triaxial fatigue cyclic and confining pressure unloading (FC-CPU) conditions," *Rock Mechanics and Rock Engineering*, 2020.

[23] Y. Wang, C. H. Li, H. Liu, and J. Q. Han, "Fracture failure analysis of freeze-thawed granite containing natural fracture under uniaxial multi-level cyclic loads," *Theoretical and Applied Fracture Mechanics*, vol. 110, article 102782, 2020.

[24] Y. Wang, C. Li, J. Han, and H. Wang, "Mechanical behaviours of granite containing two flaws under uniaxial increasing-amplitude fatigue loading conditions: An insight into fracture evolution analyses," *Fatigue & Fracture of Engineering Materials & Structures*, vol. 43, no. 9, pp. 2055–2070, 2020.

[25] Y. Wang, C. H. Li, and J. Q. Han, "On the effect of stress amplitude on fracture and energy evolution of pre- flawed granite under uniaxial increasing-amplitude fatigue loads," *Engineering Fracture Mechanics*, vol. 240, article 107366, 2020.

[26] Y. Wang, W. K. Feng, H. J. Wang, C. H. Li, and Z. Q. Hou, "Rock bridge fracturing characteristics in granite induced by freeze-thaw and uniaxial deformation revealed by AE monitoring and post-test CT scanning," *Cold Regions Science and Technology*, vol. 177, article 103115, 2020.

[27] T. Wang, Z. Liu, Y. Gao, X. Ye, and Z. Zhuang, "Theoretical and numerical models for the influence of debonding on the interaction between hydraulic fracture and natural fracture," *Engineering Computations*, vol. 36, no. 8, pp. 2673–2693, 2019.

[28] H. Yao, Z. Zhang, and D. Li, "Experimental study on the permeability characteristics of sandstone in different chemical solutions," *KSCE Journal of Civil Engineering*, vol. 22, no. 9, pp. 3271–3277, 2018.

[29] C. Y. Zhang, P. Zou, Y. X. Wang, T. T. Jiang, and P. Cao, "An elasto-visco-plastic model based on stress functions for deformation and damage of water saturated rocks during the freezing-thawing process," *Construction and Building Materials*, vol. 250, article 118862, 2020.

[30] R. H. Cao, R. B. Yao, J. J. Meng, Q. B. Lin, H. Lin, and S. Li, "Failure mechanism of non-persistent jointed rock-like specimens under uniaxial loading: Laboratory testing," *International Journal of Rock Mechanics and Mining Sciences*, vol. 132, article ???, 2020.

[31] R. H. Cao, R. B. Yao, T. Hu, C. S. Wang, K. H. Li, and J. J. Meng, "Failure and mechanical behavior of transversely isotropic rock under compression-shear tests: laboratory testing and numerical simulation," *Engineering Fracture Mechanics*, vol. 241, article 107389, 2021.

[32] R. H. Cao, C. S. Wang, R. B. Yao et al., "Effects of Cyclic Freeze-thaw Treatments on the Fracture Characteristics of Sandstone under Different Fracture Modes: Laboratory Testing," *Theoretical and Applied Fracture Mechanics*, vol. 109, article ???, 2020.

[33] Y. X. Wang, S. B. Shan, C. S. Zhang, and P. P. Guo, "Seismic response of tunnel lining structure in a thick expansive soil stratum," *Tunnelling and Underground Space Technology*, vol. 88, pp. 250–259, 2019.

[34] Y. Chen, G. P. Wen, and J. H. Hu, "Analysis of deformation characteristics of fully grouted rock bolts under pull-and shear loading," *Rock Mechanics and Rock Engineering*, vol. 53, no. 7, pp. 2981–2993, 2020.

[35] Y. L. Zhao, L. Y. Zhang, J. Liao, W. J. Wang, Q. Liu, and L. Tang, "Experimental study of fracture toughness and subcritical crack growth of three rocks under different environments," *International Journal of Geomechanics*, vol. 20, no. 8, article 04020128, 2020.

[36] Y. L. Zhao, L. Y. Zhang, W. J. Wang, Q. Liu, L. M. Tang, and G. Cheng, "Experimental study on shear behavior and a

revised shear strength model for infilled rock joints," *International Journal of Geomechanics*, vol. 20, no. 9, article 04020141, 2020.

[37] Y. L. Zhao, C. S. Zhang, Y. X. Wang, and H. Lin, *Shear-Related Roughness Classification and Strength Model of Natural Rock Joint Based on Fuzzy Comprehensive Evaluation*, International Journal of Rock Mechanics and Mining Sciences, 2021, (Available online).

[38] Y. L. Zhao, C. L. Wang, and J. Bi, "Analysis of fractured rock permeability evolution under unloading conditions by the model of elastoplastic contact between rough surfaces," *Rock Mechanics and Rock Engineering*, vol. 53, no. 12, pp. 5795–5808, 2020.

[39] S. J. Xie, H. Lin, Y. F. Chen, R. Yong, W. Xiong, and S. du, "A damage constitutive model for shear behavior of joints based on determination of the yield point," *International Journal of Rock Mechanics and Mining Sciences*, vol. 128, article ???, 2020.

[40] S. J. Xie, H. Lin, Y. X. Wang et al., "A statistical damage constitutive model considering whole joint shear deformation," *International Journal of Damage Mechanics*, vol. 29, no. 6, pp. 988–1008, 2020.

[41] Y. Zheng, C. Chen, F. Meng, H. N. Zhang, K. Z. Xia, and X. B. Chen, "Assessing the stability of rock slopes with respect to block-flexure toppling failure using a force-transfer model and genetic algorithm," *Rock Mechanics and Rock Engineering*, vol. 53, no. 8, pp. 3433–3445, 2020.

[42] Y. Zheng, C. Chen, F. Meng, T. Liu, and K. Xia, "Assessing the stability of rock slopes with respect to flexural toppling failure using a limit equilibrium model and genetic algorithm," *Computers and Geotechnics*, vol. 124, article 103619, 2020.

[43] Y. Zheng, C. Chen, T. Liu, H. Zhang, and C. Sun, "Theoretical and numerical study on the block-flexure toppling failure of rock slopes," *Engineering Geology*, vol. 263, article 105309, 2019.

[44] Y. Zheng, C. Chen, T. Liu, D. Song, and F. Meng, "Stability analysis of anti-dip bedding rock slopes locally reinforced by rock bolts," *Engineering Geology*, vol. 251, pp. 228–240, 2019.

[45] Y. Zheng, C. Chen, T. Liu, H. Zhang, K. Xia, and F. Liu, "Study on the mechanisms of flexural toppling failure in anti-inclined rock slopes using numerical and limit equilibrium models," *Engineering Geology*, vol. 237, pp. 116–128, 2018.

[46] Y. F. Chen and H. Lin, "Consistency analysis of Hoek-Brown and equivalent Mohr-coulomb parameters in calculating slope safety factor," *Bulletin of Engineering Geology and the Environment*, vol. 78, no. 6, pp. 4349–4361, 2019.

[47] H. Lin, H. Yang, Y. X. Wang, Y. L. Zhao, and R. H. Cao, "Determination of the stress field and crack initiation angle of an open flaw tip under uniaxial compression," *Theoretical and Applied Fracture Mechanics*, vol. 104, article ???, 2019.

[48] X. Fan, Z. Yang, and K. Li, "Effects of the lining structure on mechanical and fracturing behaviors of four-arc shaped tunnels in a jointed rock mass under uniaxial compression," *Theoretical and Applied Fracture Mechanics*, vol. 112, article 102887, 2021.

[49] J. J. Meng, X. Zhang, J. S. Huang, H. X. Tang, H. Mattsson, and J. Laue, "A smoothed finite element method using second-order cone programming," *Computers and Geotechnics*, vol. 123, article ???, 2020.

[50] F. Wang, P. Cao, Y. X. Wang, R. Q. Hao, J. J. Meng, and J. L. Shang, "Combined effects of cyclic load and temperature fluctuation on the mechanical behavior of porous sandstones," *Engineering Geology*, vol. 266, article ???, 2020.

[51] K. H. Li, Y. Cheng, Z. Y. Yin, D. Han, and J. J. Meng, "Size effects in a transversely isotropic rock under Brazilian tests: laboratory testing," *Rock Mechanics and Rock Engineering*, vol. 53, no. 6, pp. 2623–2642, 2020.

[52] K. H. Li, Z. Y. Yin, Y. M. Cheng, P. Cao, and J. J. Meng, "Three-dimensional discrete element simulation of indirect tensile behaviour of a transversely isotropic rock," *International Journal for Numerical and Analytical Methods in Geomechanics*, vol. 44, no. 13, pp. 1812–1832, 2020.

[53] C. Y. Zhang, C. Z. Pu, R. H. Cao, T. T. Jiang, and G. Huang, "The stability and roof-support optimization of roadways passing through unfavorable geological bodies using advanced detection and monitoring methods, among others, in the Sanmenxia Bauxite Mine in China's Henan Province," *Bulletin of Engineering Geology and the Environment*, vol. 78, no. 7, pp. 5087–5099, 2019.

[54] H. Lin, D. Lei, R. Yong, C. Jiang, and S. Du, "Analytical and numerical analysis for frost heaving stress distribution within rock joints under freezing and thawing cycles," *Environmental Earth Sciences*, vol. 79, no. 12, p. 305, 2020.

[55] H. Lin, X. Zhang, R. Cao, and Z. Wen, "Improved nonlinear Burgers shear creep model based on the time-dependent shear strength for rock," *Environmental Earth Sciences*, vol. 79, p. 149, 2020.

[56] Z. M. He, D. Xiang, Y. X. Liu, Q. F. Gao, and H. B. Bian, "Deformation behavior of coarse-grained soil as an embankment filler under cyclic loading," *Advances in Civil Engineering*, vol. 2020, Article ID 4629105, 2020.

[57] Z. M. He, Z. F. Liu, X. H. Liu, and H. B. Bian, "Improved method for determining active earth pressure considering arching effect and actual slip surface," *Journal of Central South University*, vol. 27, no. 7, pp. 2032–2042, 2020.

[58] R. Jiang, F. Dai, Y. Liu, and A. Li, *Fast Marching Method for Microseismic Source Location in Cavern-Containing Rockmass: Performance Analysis and Engineering Application*, Engineering, 2021.

[59] X. Fan, X. D. Jiang, Y. X. Liu, H. Lin, K. H. Li, and Z. M. He, "Local stress distribution and evolution surrounding flaw and opening within rock block under uniaxial compression," *Theoretical and Applied Fracture Mechanics*, vol. 112, article 102914, 2021.